Yashwanth Tummala
Graduate Research Assistant
The Pennsylvania State University,
Department of Mechanical & Nuclear Engineering,
University Park, PA 16802
e-mail: yashwanth.tummala@gmail.com

Aimy Wissa
Department of Aerospace Engineering,
University of Maryland,
National Institute of Aerospace,
Hampton, VA
e-mail: aimy.wissa@gmail.com

Mary Frecker
Professor
Department of Mechanical and
Nuclear Engineering,
The Pennsylvania State University,
University Park, PA
e-mail: mxf36@engr.psu.edu

James E. Hubbard
Langley Distinguished Professor
Department of Aerospace Engineering,
University of Maryland,
National Institute of Aerospace,
Hampton, VA
e-mail: james.hubbard@nianet.org

Design and Optimization of a Contact-Aided Compliant Mechanism for Passive Bending

A contact-aided compliant mechanism (CCM) called a compliant spine (CS) is presented in this paper. It is flexible when bending in one direction and stiff when bending in the opposite direction, giving it a nonlinear bending stiffness. The fundamental element of this mechanism is a compliant joint (CJ), which consists of a compliant hinge (CH) and contact surfaces. The design of the compliant joint and the number of compliant joints in a compliant spine determine its stiffness. This paper presents the design and optimization of such a compliant spine. A multi-objective optimization problem with three objectives is formulated in order to perform the design optimization of the compliant spine. The goal of the optimization is to minimize the peak stress and mass while maximizing the deflection, subject to geometric and other constraints. Flapping wing unmanned air vehicles, also known as ornithopters, are used as a case study in this paper to test the accuracy of the design optimization procedure and to prove the efficacy of the compliant spine design. The optimal compliant spine designs obtained from the optimization procedure are fabricated, integrated into the ornithopter's wing leading edge spar, and flight tested. Results from the flight tests prove the ability of the compliant spine to produce an asymmetry in the ornithopter's wing kinematics during the up and down strokes.
[DOI: 10.1115/1.4027702]

1 Introduction

CCMs are a class of compliant mechanisms in which the compliant members come into contact with one another to perform a specific task or to improve the performance of the mechanism itself. A wide variety of contact interactions, ranging from a simple case involving single point contact to the more complex case of multiple contacts between different parts of the compliant mechanism itself, can be used to perform special tasks. CCMs were first introduced in the literature by Mankame and Ananthasuresh [1]. Such mechanisms can have nonlinear stiffness [2–4], stress relief capabilities [5,6] and can also generate a nonsmooth path [1]. Mankame and Ananthasuresh have presented a displacement delimited contact-aided compliant gripper with a single contact point [1]. They have also presented a CCM which uses intermittent contacts to convert reciprocating translation into two output curves that enclose a two dimensional region [7]. Other CCMs that trace prescribed nonsmooth paths in response to a single monotonically increasing input force, were also synthesized by the same authors using topology optimization [8]. Reddy et al. designed CCMs to trace large, nonsmooth paths using topology optimization, and large deformation finite element analysis (FEA) [9]. Mehta et al. have designed honeycomb cells with contact elements called contact-aided cellular compliant mechanisms (C3Ms) to obtain stress relief [6,10]. Cirone et al. have designed these C3Ms with curved walls for high strain applications [11]. Halverson et al. have designed a bi-axial CCM for spinal arthroplasty [12,13]. Finally Cannon and Howell designed a contact-aided compliant revolute joint [14].

The goal of this research is to design CCMs that are capable of 3 degrees of freedom (DOF) motion, namely in-plane bending, out of plane bending or sweep, and twist. As a first step towards this goal, the focus of this paper is to present the design and optimization of a 1 DOF, namely in-plane bending compliant mechanism called a compliant spine (CS). This mechanism has nonlinear bending stiffness. The compliant spine was integrated into flapping wing unmanned air vehicle or an ornithopter to validate the efficacy of the design in achieving a desired bending deflection under a given load. During flapping wing flight, the wing motion is oscillatory and the wings' loads change directions due to flapping. Thus ornithopters can be used to verify the nonlinear stiffness capabilities of the compliant spine during the up and down strokes. Research has shown the benefits of wing morphing for flapping wing unmanned air vehicles [15]. Natural flyers achieve superior performance during flight because they use a set of wing kinematics called the continuous vortex gait (CVG) to produce lift and thrust. During the CVG, wings are fully extended during downstroke and they bend, sweep and twist during upstroke [16]. The bird's "wrist" is the joint that is responsible for this 3 DOF motion. The compliant spine presents a viable mechanism for mimicking the function of the avian wrist and achieving passive wing morphing. Passive wing morphing is defined where the wing shape change occurs due to the loads encountered by the wings during flight not due to an external set of actuators. The compliant spine, as mentioned before, is capable of 1 DOF motion, namely bending, however future mechanisms will be designed to achieve multiple degrees of freedom. The AeroVironment design, presented in Ref. [17], uses wing rotation and twist mechanisms to achieve roll, pitch and yaw control.

Contributed by the Mechanisms and Robotics Committee of ASME for publication in the Journal of Mechanisms and Robotics. Manuscript received September 10, 2013; final manuscript received April 14, 2014; published online June 17, 2014. Assoc. Editor: Anupam Saxena.

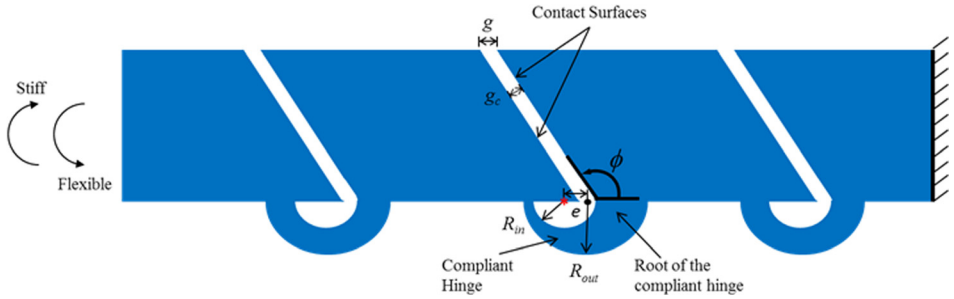

Fig. 1 Schematic of a CS with geometric parameters is shown. This mechanism is flexible when it is bent in the flexible direction and is very stiff when it is bent in the stiff direction. Performance of the CJ in the "stiff direction" is dependent on ϕ and g_c while performance of the CJ in the "flexible direction" is dependent on R_{in}, R_{out}, and e.

These mechanisms are hybrid mechanisms, i.e., they have both passive and active components. The design of these mechanisms is based on previous experiences and trial and error methods rather than a numerical optimization approach, which was used to design the compliant spine discussed in this paper [17].

The remainder of this paper is organized as follows. Section 2 introduces the compliant spine design and the geometric parameters that affect its stiffness. Section 3 presents the concomitant design optimization problem that was formulated. Design optimization results for an ornithopter test platform are presented as a case study in Sec. 4. The compliant spines obtained from the design optimization for the ornithopter application were then fabricated and flight tested successfully. Section 5 presents an overview of the flight test and its results. Finally, conclusions are drawn and future work is discussed in Sec. 6.

2 Geometeric Parameters of a Compliant Spine

A compliant spine is a monolithic contact-aided compliant mechanism with nonlinear bending stiffness. A schematic of a compliant spine is shown in Fig. 1. This mechanism is stiff in the "stiff direction," because the surfaces of the mechanism come into contact with one another and it acts like a solid beam. On the other hand, the CS is flexible in the "flexible direction," because of the semicircular compliant hinges. In this paper, upstroke is used to denote the 'flexible direction' of the CS while downstroke is used to denote the "stiff direction" of the CS. A stiffness curve of a compliant spine is shown in Fig. 2. This compliant spine was analyzed in ANSYS using quasi-static, large deformation analysis, to determine its stiffness properties and also to confirm the nonlinear stiffness behavior. Tip loads were applied in the flexible and stiff directions. During the quasi-static analysis, Solid45 elements and multilinear material properties of Delrin (Dupont polymer) were used [18,19]. Contact elements (CONTA173 and TARGE170) were used to simulate contact between the contact surfaces. Compared to the stiffness of a CS, stiffness of a rigid spar and torsional spring is expected to be linear in nature.

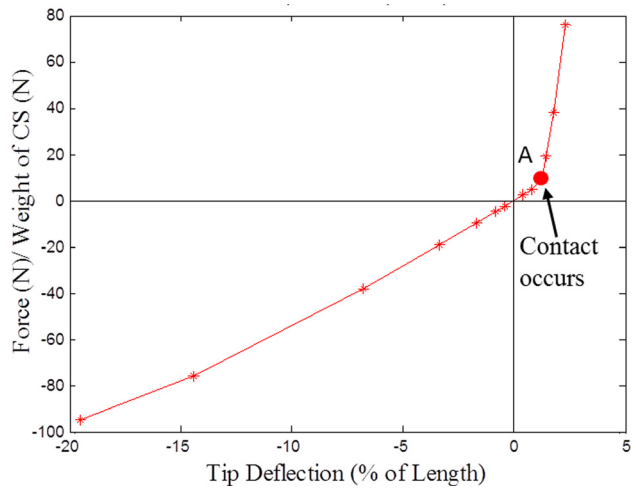

Fig. 2 Stiffness plot of a CS showing nonlinear force-deflection curve

The stiffness of a compliant spine depends on the geometry and number of compliant joints (CJs). A schematic of a single CJ is shown in Fig. 1. The stiffness of a CJ during upstroke is defined by the geometry of the CH, as shown in Fig. 1. The inner and outer surfaces of the compliant hinge are assumed to be semicircles. The choice of the semicircular shape was based on an earlier shape optimization procedure performed on a compliant hinge. In this procedure, the shape of the compliant hinge was defined by 38 control points, 19 points each for inner and outer curves. The radial coordinates were used as variables and the optimization result suggested that these curves should be approximated as semicircles. Details of this procedure can be found in Refs. [2,15]. Further, elliptical shapes could add mass to the compliant spine and some generic splines could be difficult to fabricate. The stiffness of the CJ during downstroke is defined by the contact surfaces.

The contact gap is defined as the perpendicular distance (shown as g_c in Fig. 1) between the contact surfaces. The parameter g, shown in Fig. 1, is the horizontal distance between the contact surfaces and is related to the contact gap g_c, given by Eq. (1). The contact angle of a CJ (shown as ϕ in Fig. 1) is the angle between the horizontal line drawn at the root of the compliant hinge and the contact surface closest to the CH root. Hence, the design parameters that affect the performance of a compliant joint are contact angle (ϕ), contact gap (g_c), inner radius of the compliant hinge (R_{in}), outer radius of the compliant hinge (R_{out}), and eccentricity of the compliant hinge (e). The black dot in the figure represents the center of the outer semicircle while the red star represents the center of the inner semicircle of the compliant hinge. The value of the eccentricity e is positive if the black dot is to the right of the red star and is negative if it is otherwise, except when the black dot and red star coincide; then it has a value of zero. By varying these design parameters, numerous compliant joints can be created. The performance of the compliant spine is determined by the number of compliant joints and the design of each CJ, which includes the above mentioned five parameters for each CJ. Therefore, to design a CS for upstroke, a design optimization procedure is formulated and presented in Sec. 3. This procedure is applied to an ornithopter application as a case study and the results are presented later in the paper.

$$g_c = g * \sin(180\,\text{deg} - \phi) \tag{1}$$

3 Design Optimization of a Compliant Spine

The effects of the magnitudes of the contact gap and contact angle on the downstroke performance of a single compliant joint were studied and presented in Ref. [4]. With the shape of the CH fixed, it was found that for minimum downstroke deflection of a CJ, the contact angle (ϕ) must be 130 deg and that the contact gap (g_c) in a CJ must be as small as possible. The minimum contact gap size was determined by the manufacturing process used to fabricate the CS. All of the compliant spine designs were fabricated using a water jet cutter, and based on the kerf width of the water jet, the minimum possible value of g was found to be 300 μm. This value of g was thus fixed for all CS designs.

With the contact angle and gap fixed, only three parameters remained as variables, the inner radius, outer radius, and the eccentricity of the compliant hinge. These three design parameters dictated the geometry of a single compliant joint, and affected the upstroke performance. In addition to the compliant hinge geometry, the number of compliant joints also affected the upstroke performance of a CS. Therefore, the optimization was performed using three variables per CJ ($R_{k\,\text{in}}$, $R_{k\,\text{out}}$, and e_k) and the total number of design variables was three times the number of compliant joints (T). The optimization problem was solved for a fixed number of compliant joints, selected by the designer.

A multi objective optimization problem was formulated to minimize the mass of the CS (f_1) and the peak stress experienced during upstroke (f_3), while maximizing the tip deflection (f_2) during upstroke, as shown below:

$$\begin{gathered}\text{Minimize } (f_1, f_3)\\ \text{Maximize } (f_2)\end{gathered}$$

S.T.

$$\left.\begin{gathered}R_{\boldsymbol{k}\,\text{in}} - R_{\boldsymbol{k}\,\text{out}} + |e_{\boldsymbol{k}}| \le 0\\ \text{lb}_{\text{in}} \le R_{\boldsymbol{k}\,\text{in}} \le \text{ub}_{\text{in}}\\ \text{lb}_{\text{out}} \le R_{\boldsymbol{k}\,\text{out}} \le \text{ub}_{\text{out}}\\ \text{lb}_e \le e_{\boldsymbol{k}} \le \text{ub}_e\end{gathered}\right\} \boldsymbol{k} = 1, 2, 3, \ldots, T \tag{2}$$

where

$$f_1 = \lambda * M + (1 - \lambda) * M_{\text{penalty}} \tag{3}$$

$$f_2 = \lambda * Z_{\max} - (1 - \lambda) * Z_{\text{penalty}} \tag{4}$$

$$f_3 = \lambda * \sigma_{\max} + (1 - \lambda) * \sigma_{\text{penalty}} \tag{5}$$

$$\lambda = \begin{cases} 1 \text{ if } \sigma_{\max} \le \sigma_{\text{cutoff}} \\ 0 \text{ if } \sigma_{\max} > \sigma_{\text{cutoff}} \end{cases} \tag{6}$$

$$\sigma_{\text{cutoff}} = \alpha * \sigma_{\text{yield}} \tag{7}$$

$$M_{\text{penalty}} \gg M \tag{8}$$

$$Z_{\text{penalty}} \ll Z_{\max} \tag{9}$$

$$\sigma_{\text{penalty}} \gg \sigma_{\max} \tag{10}$$

Geometric constraints on the design variables, given by Eq. (2), ensured that the inner and outer semicircles of the hinges never intersect, thus ensuring geometrically feasible compliant hinges. The variables lb_{in} and ub_{in} are the lower and upper bounds on the inner radius ($R_{k\,\text{in}}$) of **k**th compliant hinge. CJs were counted starting from the tip to the root. The variables lb_{out} and ub_{out} are the lower and upper bounds on the outer radius ($R_{\boldsymbol{k}\,\text{out}}$) of **k**th compliant hinge, and the variables lb_e and ub_e are the lower and upper bounds on the eccentricity ($e_{\boldsymbol{k}}$) of **k**th compliant hinge. The objective functions f_1, f_2, and f_3, given by Eqs. (3)–(5), respectively, were calculated using a commercial finite element package, ANSYS. The loading conditions used to calculate $Z_{\max}$ and $\sigma_{\max}$ in objectives f_2 and f_3, respectively, are described in the Sec. 4. The mass (M) used to calculate objective f_1 is simply the product of the volume and material density.

An effective approach to solving this optimization problem was to use a heuristic optimization algorithm like the multi-objective evolutionary algorithms (MOEAs). Zhou et al. present a survey of the state of the art MOEAs [20]. A controlled elitist genetic algorithm (GA), which is a variant of NSGA-II [21,22], was used for the optimization here. This GA is part of the optimization toolbox provided in MATLAB.

Constraints on the objective functions were imposed using the penalty values M_{penalty}, Z_{penalty}, and σ_{penalty} and the binary variable λ. These penalty values (Eqs. (8)–(10)) were chosen such that an infeasible design, determined by Eq. (6), is assigned a poor value of the objective function. Such designs were terminated and not allowed to propagate into future generations. These penalty values were chosen based on experience and generally need to be at least five orders of magnitude greater than the values of the objective functions. Computation time was also an important factor in this optimization because each CS design in every generation was being evaluated individually using FEA. Taking the computational resources and complexity of the problem into consideration, penalty values have proven to be very effective in driving the optimization towards feasible regions in the design space. A CS design was considered to be infeasible if the maximum von Mises stress ($\sigma_{\max}$) in the design, during dynamic analysis is greater than a cutoff stress limit (σ_{cutoff}), calculated from Eq. (7). This limit, which was a function of yield stress of the material (σ_{yield}), is set by the designer when choosing an appropriate value for α, which can be a function of the safety factor.

The optimization problem was implemented as shown in Fig. 3. The optimization procedure was stopped when convergence is achieved. Convergence of this multi-objective optimization problem was determined using the convergence metric proposed by Deb and Jain [23]. This metric, as was shown in Ref. [23], is a measure of the average distance between the reference set and the nondominated population members of each of the generations;

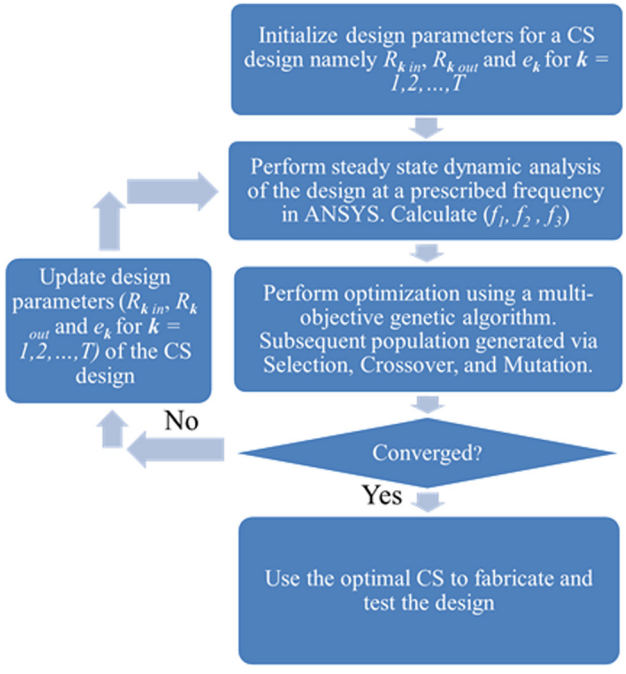

Fig. 3 Flow diagram showing steps involved in solving the multi-objective optimization problem. NSGA-II (genetic algorithm) is used to solve this optimization problem.

Table 1 Parameters used in the CS optimization

Variable	Value
α	1
σ_{yield}	45×10^6 Pa
ϕ	130 deg
g	300 μm
lb_{in}	0.0004 m
ub_{in}	0.005 m
lb_{out}	0.0004 m
ub_{out}	0.005 m
lb_e	−0.004 m
ub_e	0.004 m
$M_{penalty}$	14.2×10^6 kg
$Z_{penalty}$	1000 m
$\sigma_{penalty}$	$10{,}000 \times 10^6$ Pa
P_{size}	100
ρ_{delrin}	1420 kg/m^3
M_{max}	0.0145 kg

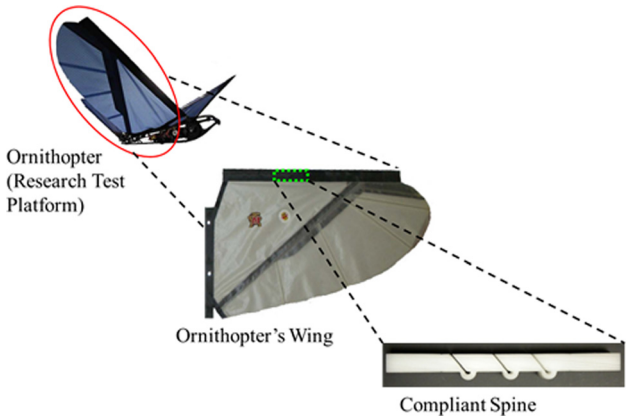

Fig. 4 Ornithopter research test platform with a wing span of 1.06 m is shown here. The CS is inserted in the leading edge spar at 37% of the half wing span. The CS imitates the function of an avian wrist, thus enabling passive bending during upstroke.

this average distance was normalized to always lie between 0 and 1. The optimization was said to have converged when the actual average distance is less than 0.06. This design optimization procedure along with the convergence metric was implemented for CSs for an ornithopter application and the optimization results are shown in Sec. 4.

4 Design Optimization Case Study: Avian-Scale Ornithopter

This section discusses the details of a test ornithopter that was used as a case study to set the constraints and inputs to the design optimization procedure discussed in Sec. 3. The values of the parameters used are given in Table 1. The avian-scale ornithopter application imposed dimensional constraints on the CS designs, as it was based on an actual 1.06 m wingspan test platform [24], as shown in Fig. 4. The CS was inserted in the leading edge spar of the ornithopter's wing at the wrist location (37% of half wing span), as shown in Fig. 4. To be compatible with the leading edge spar and wing membrane of the test platform, the CS design was no larger than 63.5 mm × 12.7 mm × 12.7 mm. These dimensional constraints limited the number of compliant joints that can be accommodated in a single CS. Hence CSs with two, three and four compliant joints were optimized using the design optimization procedure. A larger number of compliant joints would exceed

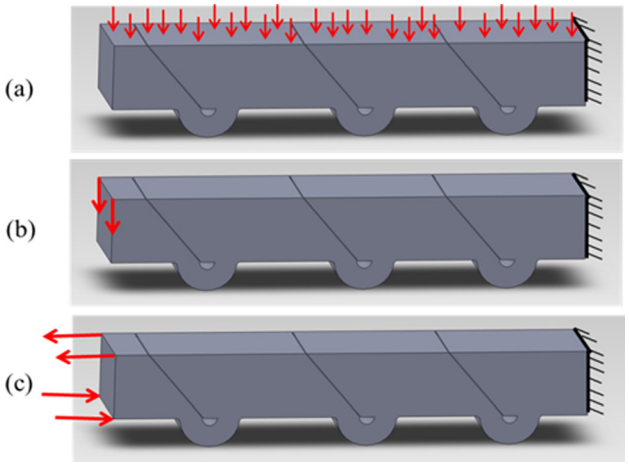

Fig. 5 Different loading conditions used during CS optimization. (*a*) Distributed loads, (*b*) tip loads, (*c*) pure moments. All of these loading conditions were used during the design optimization procedure to understand the effect of different loading conditions on optimal CS designs.

the allowable length. The results of the optimization are presented in this section. A two compliant jointed compliant spine (CJCS) is defined as a compliant spine with two compliant joints. Similarly, a three CJCS is a compliant spine with three compliant joints, and so on. This terminology will be used from here on in this paper.

For each design and in each generation, finite element analysis was performed to calculate the objective functions and evaluate the constraints. The material was assumed to be DuPont Delrin 100ST. Delrin was chosen because of its good fatigue properties, elastic strength, manufacturability and availability. Multilinear isotropic material properties of Delrin were used during the analysis; the yield strength was assumed to be 45 MPa [18,19]. SOLID 45 elements (3D finite elements in ANSYS) were used to mesh the CS designs.

During the finite element analysis, the loads experienced by the compliant spine must be taken into account. The aerodynamic load distribution encountered during the flapping cycle was not well quantified, but it was known that the wing loads experienced by the ornithopter during lift generation cause both bending and shear in the CSs. The relative contribution of the bending moment and shear to the actual loading distribution were unknown. We have considered three different loading conditions to approximate the actual load distribution, as shown in Fig. 5. They were aerodynamic lift loads during upstroke approximated as (a) uniform pressure acting on the top surface of the CSs (Fig. 5(*a*)), (b) tip loads (Fig. 5(*b*)), (c) pure moments at the tip (Fig. 5(*c*)). All these three loading conditions were applied on two, three and four CJCS. The ends of the CSs at the roots were fixed. In all cases a steady-state dynamic analysis was performed to simulate the upstroke condition. The forcing frequency (ω) of the applied dynamic load was 5 Hz, corresponding to the flapping frequency of steady level flight for the test ornithopter [4,24].

A conservative design approach was taken to approximate the magnitude of the dynamic load. Based on previous experimental and simulation analysis, the details of which were presented in Refs. [3,24], the magnitude of the maximum tip load at mid-upstroke was approximated to be 10 N. Using this as a basis, a more conservative loading pattern (pure moment) and a less conservative loading pattern (distributed load) were used to analyze the CSs. For the distributed loading condition, the uniform pressure applied on the top surface of a CS was obtained by dividing 10 N with the total surface area on the top surface of the CS. For the pure moment case, the moment observed at the root of the CS (10 N * length of the CS) during a tip loading condition was

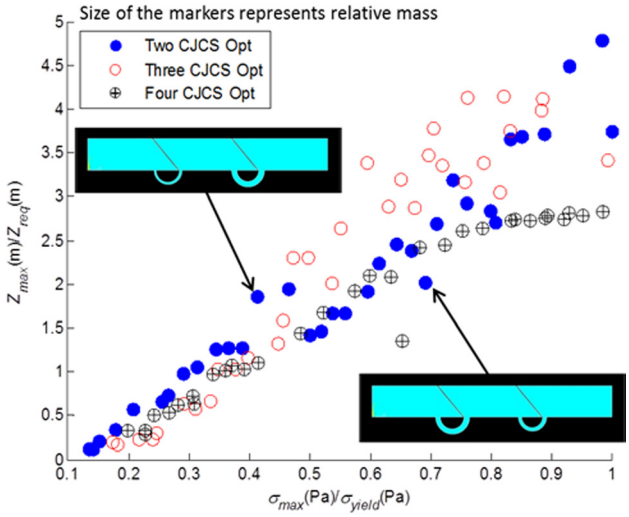

Fig. 6 Pareto plot comparing deflection and maximum von Mises stress for distributed loads. Size of the circles represents relative mass. All the optimal designs have thin CHs.

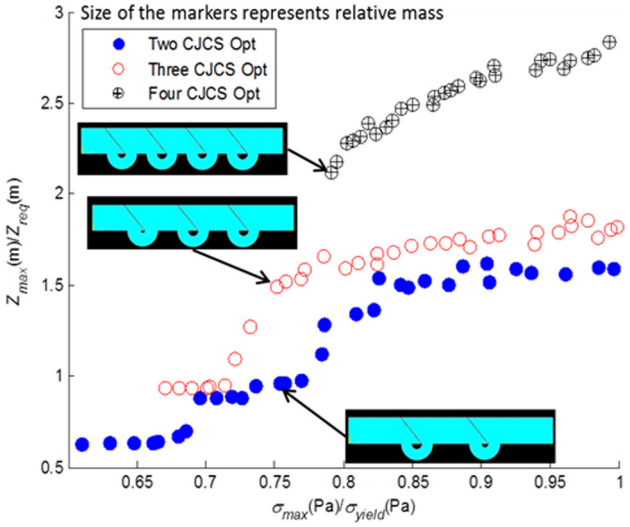

Fig. 8 Pareto plot comparing deflection and maximum von Mises stress for pure moment loads. Optimal designs in this case have the least, maximum possible tip deflections, (only about 2.84*Z_{req}) amongst the three loading conditions.

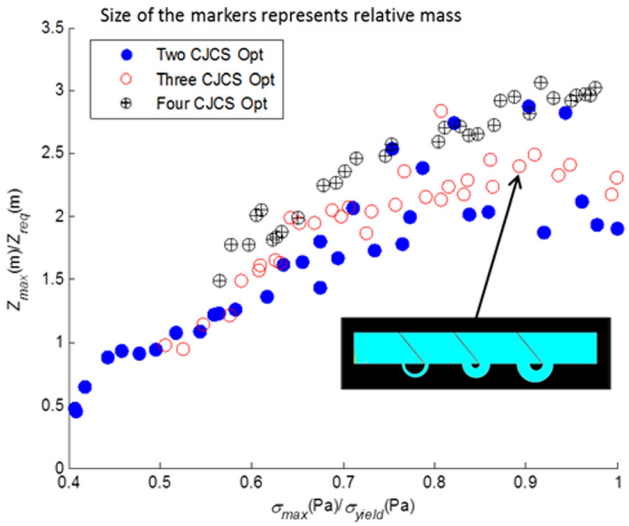

Fig. 7 Pareto plot comparing deflection and maximum von Mises stress for tip loads. Many of the optimal CSs designs have a very thin CH close to the tip.

chosen to be applied as a uniform moment. The length of all the CSs is 63.5 mm. Hence, a pure bending moment of magnitude 0.635 Nm was applied.

Optimization results obtained from each of these loading conditions are shown in Figs. 6–8. Each of these plots show the Pareto fronts obtained. Since this was a multi-objective optimization problem with three objectives, the axes of the plots compares two of the normalized objectives, tip deflection and stress, while the size of the markers represents the normalized mass. The bending tip deflection (Z_{max}) was normalized with the desired tip deflection (Z_{req}). As presented in Ref. [3], the CSs were assumed to require a tip deflection of at least 8.42 mm. The maximum von Mises stress (σ_{max}) observed was normalized with the yield stress of Delrin (σ_{yield}) and the mass was normalized with the mass of a Delrin^{TM} block with dimensions 63.5 mm × 12.7 mm × 12.7 mm. A good design in these plots would be near the upper left hand corner with a small marker size. A design is considered good when it has minimum mass, maximum displacement, and minimum stress. Hence, a good design is expected to have a small marker size and be located near the upper left hand corner of the plot shown in Fig. 6.

All of the compliant joints of optimal CSs obtained from the distributed loads case had thin compliant hinges and hence larger deflections (shown in Fig. 6). This was because the load is uniformly distributed across the length of the CS and as a result the moment acting at each of the joints was relatively small compared to the other two cases. Since two of the objectives were to maximize tip bending deflection and minimize mass, the algorithm tended to converge to solutions with thinner CHs for all the compliant joints.

A different trend was observed in the Pareto front of the CSs obtained by using tip loads. In this case, the CHs at the root of the CS were thick but the CHs at the tip were thin (shown in Fig. 7). This was because the bending moment caused by the tip loads was lower near the tip of the CS. Since one of the objectives was to maximize bending deflection, and the CH closest to the tip experiences very small bending moment, the hinges tend to be thinner. In other words, the induced stress because of the bending moment was higher at the root than at the tip. As a result CHs close to the root were thick. At the same time, because deflection was being maximized and stresses close to the tip were not very high, the CH close to the tip could be made flexible and the optimization results suggested the same. For the pure moment case, since the bending moment was uniform along the length of the CS, all the CHs were thick (shown in Fig. 8).

It can be seen in Figs. 6–8 that there are certain trends in the objective functions as the number of compliant joints increases. Figure 7 shows that the Pareto front of the three CJCS lies in between the Pareto fronts of four CJCS and two CJCS, and that for a particular stress, the deflection of a four CJCS is almost always more than the deflection of a two CJCS. It can also be observed that the lower left corners of Figs. 7 and 8 are dominated by the two CJCS designs (blue points). This suggests that, for pure moment and tip loading conditions, the upstroke stiffness of a design is a function of the number of joints and the minimum possible deflection is higher for a design with more number of joints.

Figure 8 suggests that four CJCS designs are generally more massive than two or three CJCS designs. There is on average, about 6% increase in the mass between two CJCS and four CJCS; this small change in mass is not particularly visible in the

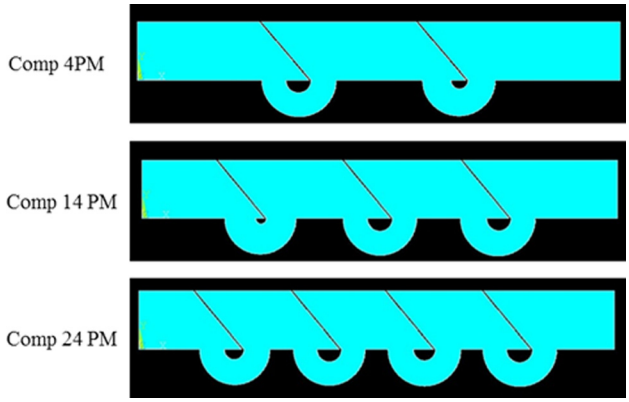

Fig. 9 Optimal CSs that were used for successful flight testing. These designs were obtained from pure moment loading conditions.

plots. It can be noted that the CS designs were being designed for an avian-scale ornithopter which weighs 0.425 kg and the mass of the CS designs is not as critical as the deflection and stress. Hence, while choosing the optimal CSs, mass was not given as much relative importance.

Optimization results suggest that although four CJCSs had greater mass than the two CJCSs and the three CJCSs, they also had greater maximum possible deflection values. If the application required a large deflection within a certain stress limit and the mass of the CS was not critical, then CJCS designs with four or more joints should be used in the optimization, i.e., a design in the upper right corner of Figs. 7 and 8 must be selected. Thus from Figs. 7 and 8, it is evident that a compliant joint adds a small amount of mass to the CS but increases the deflection, i.e., decreases its stiffness, at the same time. There is a tradeoff between the number of compliant joints (or mass) and the desired deflection. Three optimal compliant spines from these results were chosen for prototyping and flight testing purposes, details of which are presented in Sec. 5.

5 Compliant Spine Fabrication and Testing

The overall goal of the research presented in this paper, is to design a compliant spine that is able to achieve passive bending deflection while minimizing weight and without exceeding a certain stress. The ornithopter serves as an appropriate application for the compliant spine and the free flight test serves as a validation tool for the performance of the compliant spine when applied to the ornithopter case study.

Three compliant spine designs were selected for prototyping and testing purposes (Fig. 9). All three designs are based on the pure moment loading condition, since they were the most conservative with respect to stress. All these designs are predicted to have a tip deflection of at least 8.42 mm ($Z_{max}/Z_{req} > 1$) and a safety factor of approximately 1.33. Since there were no four CJCSs that had a safety factor of 1.33, a design with the least stress (design called Comp 24 PM) was chosen, shown in Figs. 8 and 9. All the three designs were attached to the leading edge spar using Delrin collars and Nylon bolts as shown in Fig. 10(*a*). As mentioned before, the CS was placed at 37% of the half wing span to mimic the function of an avian wrist. Figure 10(*b*) shows the front view of the wing with Comp 24PM in the leading edge spar.

The optimized CS designs shown in Fig. 9 were flight tested at the Wright Patterson Air Base (WPAFB) indoor flight facility [25]. During the test, a Vicon motion tracking system with 60 motion cameras was used to capture the wing kinematics. By adding small retro-reflective markers to the test vehicle, the Vicon® system can track position and orientation of the vehicle with an accuracy of about 1.0 mm. Fifty-three reflective spherical markers

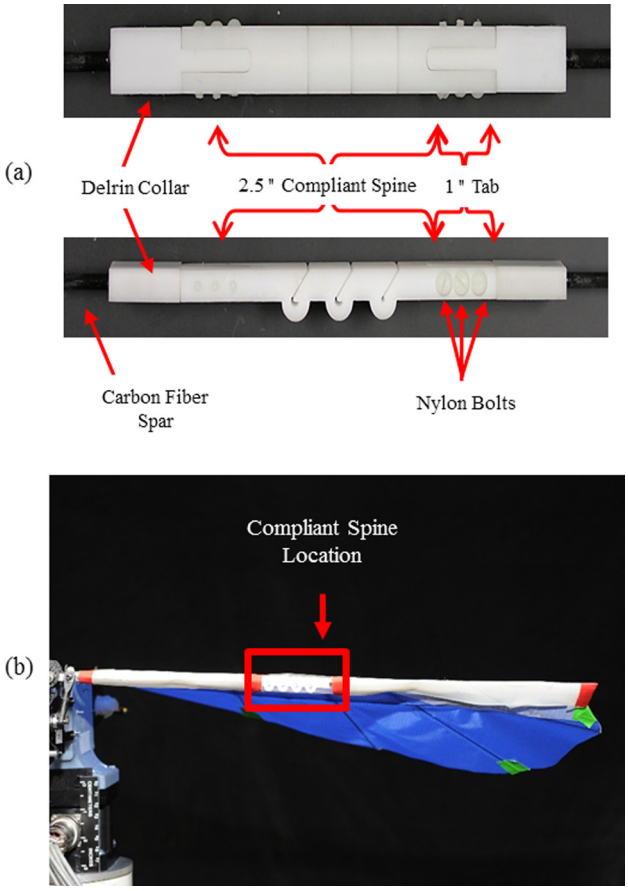

Fig. 10 (*a*) Compliant spine-spar assembly. Each design consisted of 2.5 in. of CS, 1 in. tab and a Delrin collar on each end. (*b*) A front view of the left wing, showing the location of the CS at 37% of the wing half span.

were attached to the test vehicle in locations that were necessary to obtain sufficient data to fully determine the vehicle wing and body kinematics. Out of the fifty-three markers, forty-four 6.35 mm diameter markers were placed in an asymmetrical pattern on the wings in order to aid in down range tracking. The other 9 markers were distributed as follows: 5 were placed on the fuselage to determine the ornithopter's body kinematics, 3 were placed on the tail to record user control inputs and 1 was placed at the wing root to measure the wing angle during a given flapping cycle. Data were collected at a sampling rate of 200 Hz during these tests. The Vicon® motion capture system was used to capture and contrast the wing 3D kinematics of the ornithopter with and without the compliant spine inserted in the leading edge spar.

To aid in test data repeatability and prevent vehicle impacts with the chamber walls, a low-friction tether was utilized to guide the vehicle within the test chamber. The vehicle was suspended from a lead wire hung from this tether in order to restrain its flight path. The lead line was able to slide along the tether by using a barrel swivel attachment. The tether was strung horizontally between two trusses at opposite corners of the flight lab, at 2.1 m height in order to maximize flight distance and keep the test vehicle at a height where camera coverage is ideal. The tether also prevented the vehicle from leaving the region where high speed cameras were recording the flight. A wire crimp and a braking tether were used at the end of the flight path in order to arrest the vehicle at the end of each test run. Figure 11 shows a schematic of the test setup. The flight test set-up and test protocol is described in detail in Ref. [25].

Figure 12 shows the measured X, Y, and Z positions of the 53 markers that were mounted on the ornithopter relative to the

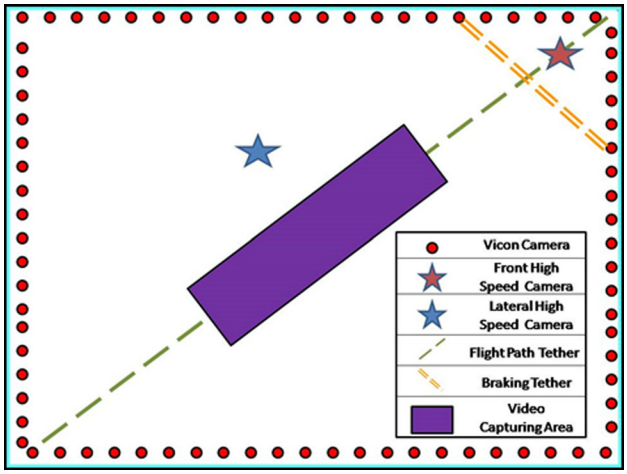

Fig. 11 Test setup schematic showing the Vicon® cameras (representative), high speed cameras, flight path, braking tether, and video capturing area

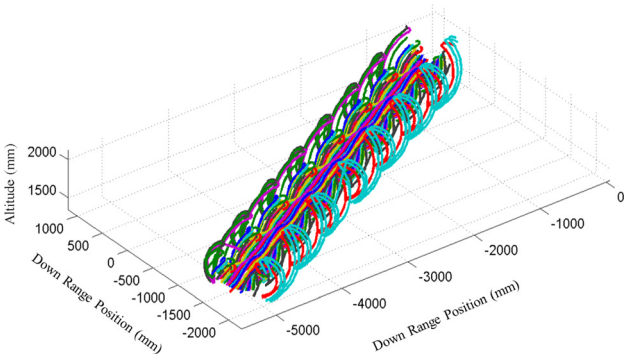

Fig. 12 *X*, *Y*, and *Z* positions of the 53 markers mounted on the ornithopter with respect to the inertial frame of reference showing over eight flapping cycles of consistent and repeatable kinematics

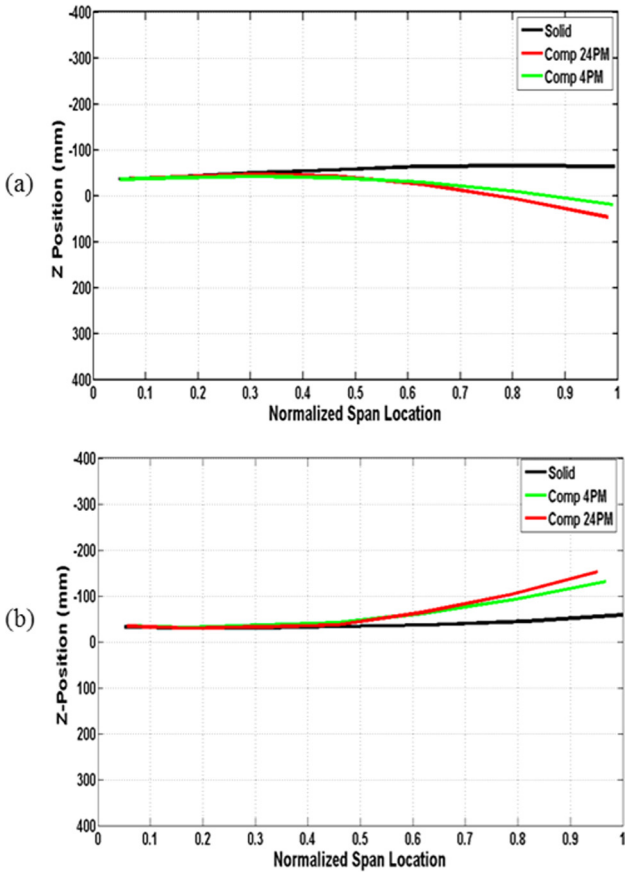

Fig. 13 The *Z* position of the reflective markers mounted at the right wing leading edge spar versus the normalized span location (*a*) at mid upstroke and (*b*) at mid downstroke

inertial reference frame. The *X* and *Y* position represents the down range location of the marker and the *Z* position represent the marker's altitude. The figure also illustrates that repeatable tracking was achieved. The plot extends over eight consistent flapping cycles and represents a duration of 1.5 s of flight data. In order to estimate the accuracy of the markers' location and tracking, the ornithopter was placed in the middle of the control volume and the variances of the markers *X*, *Y*, and *Z* locations were computed. The maximum standard deviation was calculated to be 0.10 mm, 0.10 mm, and 0.12 mm for the *X*, *Y*, and *Z* markers location, respectively.

The effect of the presence of the compliant spine on the ornithopter performance is discussed in Ref. [25]. In the current paper, the flight test is used to validate and observe the compliant spine bending deflection during both the upstroke and the downstroke. Figures 13(*a*) and 13(*b*) show the bending deflection of the markers placed on the right wing leading edge spar at mid upstroke and mid downstroke, respectively. The figures compare the leading edge spar deflection of the solid or uniform carbon fiber spar, the Comp 24PM and the Comp 4PM wing configurations. The Solid, Comp 24PM, and Comp 4PM designs were chosen for presentation because they represent the baseline, the most flexible and least flexible configurations, respectively. During the upstroke the compliant spine passively flexed because of the presence of the compliant hinges, while during the downstroke the contact surfaces came together, locking the compliant spine so that it acted like the uniform carbon fiber spar. The upstroke wing tip bending deflection observed during a previous constrained flight test [4] was found to agree with the simulation results within 6%.

Figure 13(*a*) confirms the design optimization result stating that Comp 24PM is more flexible than Comp 4PM. During upstroke, the relative bending deflection between the compliant spar tip marker and the solid spar tip marker is 110.7 mm and 83.24 mm for the Comp 24PM and Comp 4PM, respectively. In Fig. 13(*b*) shows that undesirable upwards bending occurs during the downstroke. This adverse effect is present due to the contact gaps and the flexibility of Delrin. The relative bending deflection between the compliant spar tip marker and the solid spar tip marker is 94.3 mm and 72.6 mm for the Comp 24PM and Comp 4PM, respectively.

The aforementioned test proved to be successful in producing consistent and repeatable flight data over more than eight free flight flapping cycles. It also confirmed that inserting the compliant spine into the leading edge spar introduced an asymmetry between the upstroke and the downstroke, as desired. However, the data shows that undesirable bending occurs during the downstroke due to the flexibility of Delrin and the contact gaps.

The presence of the compliant spine in the wing leading edge spar improved the overall performance of the test ornithopter at steady level flight without incurring any power penalties [25]. Comp 14PM design increased the baseline ornithopter horizontal propulsive force coefficient by 300%. A higher horizontal propulsive force coefficient indicates that for a given distance per unit time, the vehicle has more propulsive power in the horizontal direction which implies thrust gains. Also Comp 24PM design

reduced the baseline ornithopter body's center of mass positive acceleration by 69% which translates into overall vertical propulsive force gains which implies lift gains [25]. These flight tests showed that passively morphing the wings through inserting the compliant spines in the leading edge spar is not only possible and requires no additional power expenditure but it is also beneficial to the overall vertical and horizontal propulsive force production.

6 Conclusions and Future Work

A novel contact-aided compliant mechanism called compliant spine was presented, along with an optimization methodology for their design. This optimization methodology was applied to the design of compliant spines for passive wing morphing of an avian-scale ornithopter. The optimization results indicated that as the number of compliant joints in a compliant spine increased, the stiffness of the mechanism during upstroke decreased but the mass increased. Based on the results from the pure moment loading conditions, three optimal compliant spines were chosen for prototyping and testing purposes. These compliant spines were successfully flight tested. Flight testing results suggested that insertion of the CSs in an ornithopters leading edge spar caused an asymmetry between the upstroke and the downstroke. During the upstroke, the CS caused the wing to bend, however during the downstroke some undesirable bending occurred due to the flexibility of Delrin and the presence of the contact gaps. Spacing between the CJs will be considered as a geometric parameter in the future work. Future work also includes designing, optimizing, fabricating and testing of contact-aided compliant mechanisms to achieve passive bending, sweeping and twisting of the ornithopter's wings simultaneously.

Acknowledgment

The authors gratefully acknowledge the support of AFOSR grants FA9550-09-1-0632 and FA9550-13-0126 under the direction of Dr. David Stargel. The computational work was supported in part through instrumentation funded by the National Science Foundation through grant OCI–0821527. The resources of the NASA Langley Research Center, Pennsylvania State University, the University of Maryland and the Morpheus Lab are also appreciated.

Nomenclature

e = eccentricity of the compliant hinge (m)
e_k = eccentricity of the kth compliant hinge
f_1 = mass objective function in compliant spine optimization
f_2 = bending deflection objective function in compliant spine optimization
f_3 = stress objective function in compliant spine optimization
g = horizontal distance between the contact surfaces (m)
g_c = contact gap between the contact surfaces (m)
$\mathbf{k}$ = variable used to represent an compliant joint's number
lb_e = lower bound on the eccentricity of a compliant hinge
lb_{in} = lower bound on the inner radius of a compliant hinge
lb_{out} = lower bound on the outer radius of a compliant hinge
M = mass of a compliant spine design (kg)
M_{penalty} = penalty value for mass objective function (kg)
R_{in} = inner radius of a single compliant hinge (m)
$R_{k\ \text{in}}$ = inner radius of the kth compliant hinge
$R_{k\ \text{out}}$ = outer radius of the kth compliant hinge
R_{out} = outer radius of a single compliant hinge (m)
T = maximum number of compliant joint's in a compliant spine
ub_e = upper bound on the eccentricity of a compliant hinge
ub_{in} = upper bound on the inner radius of a compliant hinge
ub_{out} = upper bound on the outer radius of a compliant hinge
X = sweep direction
Y = direction along the length of a compliant spine
Z = bending direction
Z_{max} = bending tip deflection observed in a compliant spine (m)
Z_{penalty} = penalty value used for bending deflection objective function (m)
Z_{req} = minimum required bending deflection of a compliant spine
α = parameter to determine cutoff stress in the optimization, chosen by the designer
λ = binary variable
ρ_{delrin} = density of Delrin™ (kg/m^3)
σ_{cutoff} = stress limit on compliant spine designs used during compliant spine optimization (Pa)
σ_{max} = maximum von Mises stress in a compliant spine (Pa)
σ_{penalty} = penalty value for stress objective function (Pa)
σ_{yield} = yield stress of compliant spine material (Pa)
ϕ = contact angle of the compliant joint (deg)

References

[1] Mankame, N. D., and Ananthasuresh, G. K., 2002, "Contact-Aided Compliant Mechanisms: Concept and Preliminaries," ASME Paper No. DETC2002/MECH-34211.
[2] Tummala, Y., Wissa, A., Frecker, M., and Hubbard, J. E., Jr., 2010, "Design of a Passively Morphing Ornithopter Wing Using a Novel Compliant Spine," Proceedings of Smart Materials, ASME Paper No. SMASIS2010-3637.
[3] Tummala, Y., Wissa, A., Frecker, M., and Hubbard, J. E., Jr., 2011, "Design Optimization of a Compliant Spine for Dynamic Applications," ASME Paper No. SMASIS2011-5207.
[4] Wissa, A., Tummala, Y., Hubbard, J. E., Jr., and Frecker, M., 2012, "Passively Morphing Ornithopter Wings Using a Novel Compliant Spine: Design and Testing," Smart Mater. Struct., **21**(9), p. 094028.
[5] Mehta, V., Frecker, M., and Lesieutre, G., 2008, "Contact-Aided Compliant Mechanisms for Morphing Aircraft Skin," Proc. SPIE, **6926**, p. 69260C.
[6] Mehta, V., Frecker, M., and Lesieutre, G. A., 2012, "Two-Step Design of Multicontact-Aided Cellular Compliant Mechanisms for Stress Relief," ASME J. Mech. Des., **134**(12), p. 121001.
[7] Mankame, N. D., and Ananthasuresh, G. K., 2004, "A Novel Compliant Mechanism for Converting Reciprocating Translation Into Enclosing Curved Paths," ASME J. Mech. Des., **126**(4), pp. 667–672.
[8] Mankame, N. D., and Ananthasuresh, G. K., 2007, "Synthesis of Contact-Aided Compliant Mechanisms for Non-Smooth Path Generation," Int. J. Numer. Methods Eng., **69**(12), pp. 2564–2605.
[9] Reddy, B. V. S. N., Naik, S. V., and Saxena, A., 2012, "Systematic Synthesis of Large Displacement Contact-Aided Monolithic Compliant Mechanisms," ASME J. Mech. Des., **134**(1), p. 011007.
[10] Mehta, V., Frecker, M., and Lesieutre, G. A., 2009, "Stress Relief in Contact-Aided Compliant Cellular Mechanisms," ASME J. Mech. Des., **131**(9), p. 091009.
[11] Cirone, S. A., Hayes, G. R., Babcox, B. L., Frecker, M., Adair, J. H., and Lesieutre, G. A., 2012, "Design of Contact-Aided Compliant Cellular Mechanisms With Curved Walls," J. Intell. Mater. Syst. Struct., **23**(16), pp. 1773–1785.
[12] Halverson, P. A., Howell, L. L., and Bowden, A. E., 2008, "A Flexure-Based Bi-Axial Contact-Aided Compliant Mechanism for Spinal Arthroplasty," ASME Paper No. DETC2008-50121.
[13] Halverson, P. A., Howell, L. L., and Magleby, S. P., 2010, "Tension-Based Multi-Stable Compliant Rolling-Contact Elements," Mech. Mach. Theory, **45**(2), pp. 147–156.
[14] Cannon, J. R., and Howell, L. L., 2005, "A Compliant Contact-Aided Revolute Joint," Mech. Mach. Theory, **40**(11), pp. 1273–1293.
[15] Wissa, A. A., Tummala, Y., Hubbard, J. E., Jr., and Frecker, M. I., 2012, "Passively Morphing Ornithopter Wings Constructed Using a Novel Compliant Spine: Design and Testing," Smart Mater. Struct., **21**(9), p. 094028.
[16] Brown, R. H. J., 1953, "The Flight of Birds. 2. Wing Function in Relation to Flight Speed," J. Exp. Biol., **30**(1), pp. 90–103.
[17] Keennon, M., Klingebiel, K., Won, H., and Andriukov, A., 2012, "Development of the Nano Hummingbird: A Tailless Flapping Wing Micro Air Vehicle," 50th AIAA Aerospace Sciences Meeting Including the New Horizons Forum and Aerospace Exposition, Nashville, TN. January 9–12, AIAA Paper No. 2012-0588.
[18] DuPont, 2011, "Delrin: Acetal Resin," DuPont, Wilmington, DE, http://plastics.dupont.com/plastics/pdflit/americas/delrin/230323c.pdf
[19] Olympio, K. R., 2006, "Design of a Passive Flexible Skin for Morphing Aircraft Structures," M.S. thesis, The Pennsylvania State University, University Park, PA.
[20] Zhou, A., Qu, Bo-Yang, Li, H., Zhao, Shi-Zheng, Suganthan, P. N., and Zhang, Q., 2011, "Multiobjective Evolutionary Algorithms: A Survey of the State of the Art," Swarm Evol. Comput., **1**(1), pp. 32–49.

[21] Deb, K., Pratap, A., Agarwal, S., and Meyarivan, T., 2002, "A Fast and Elitist Multiobjective Genetic Algorithm: NSGA-II," IEEE Trans. Evol. Comput., **6**(2), pp. 182–197.
[22] Deb, K., 2001, *Multi-Objective Optimization Using Evolutionary Algorithms*, John Wiley & Sons, Chichester, New York.
[23] Deb, K., and Jain, S., 2002, "Running Performance Metrics for Evolutionary Multi-Objective Optimizations," 4th Asia-Pacific Conference on Simulated Evolution and Learning (SEAL'02), Singapore, November 18–22, pp. 13–20.
[24] Wissa, A., Tummala, Y., Hubbard, J. E., Jr., and Frecker, M., 2011, "Testing of Novel Compliant Spines for Passive Wing Morphing," ASME Paper No. SMASIS2011-5198
[25] Wissa, A., Guerreiro, N., Grauer, J., Hubbard, J. E., Jr., Altenbuchner, C., Tummala, Y., Frecker, M., and Roberts, R., 2013, "Flight Testing of Novel Compliant Spines for Passive Wing Morphing on Ornithopters," 21st AIAA/ASME/ASCE/AHS/ASC Structures, Structural Dynamics, and Materials Conference, Boston, MA, April 8–11.